arXiv:2408.16690v3 [cs.CV] 3 Jan 2025

Generic Objects as Pose Probes for Few-shot View Synthesis

Zhirui Gao, Renjiao Yi† , Chenyang Zhu, Ke Zhuang, Wei Chen, Kai Xu†, *Senior Member, IEEE*

***Abstract*—Radiance fields, including NeRFs and 3D Gaussians, demonstrate great potential in high-fidelity rendering and scene reconstruction, while they require a substantial number of posed images as inputs. COLMAP is frequently employed for preprocessing to estimate poses. However, COLMAP necessitates a large number of feature matches to operate effectively, and struggles with scenes characterized by sparse features, large baselines, or few-view images. We aim to tackle few-view NeRF reconstruction using only 3 to 6 unposed scene images, freeing from COLMAP initializations. Inspired by the idea of calibration boards in traditional pose calibration, we propose a novel idea of utilizing everyday objects, commonly found in both images and real life, as "pose probes". By initializing the probe object as a cube shape, we apply a dual-branch volume rendering optimization (object NeRF and scene NeRF) to constrain the pose optimization and jointly refine the geometry. PnP matching is used to initialize poses between images incrementally, where only a few feature matches are enough. PoseProbe achieves state-of-the-art performance in pose estimation and novel view synthesis across multiple datasets in experiments. We demonstrate its effectiveness, particularly in few-view and large-baseline scenes where COLMAP struggles. In ablations, using different objects in a scene yields comparable performance, showing that PoseProbe is insensitive to the choice of probe objects. Our project page is available at: https://zhirui-gao.github.io/PoseProbe.github.io/**

***Index Terms*—Neural radiance fields, few-view reconstruction, pose optimization, pose probe.**

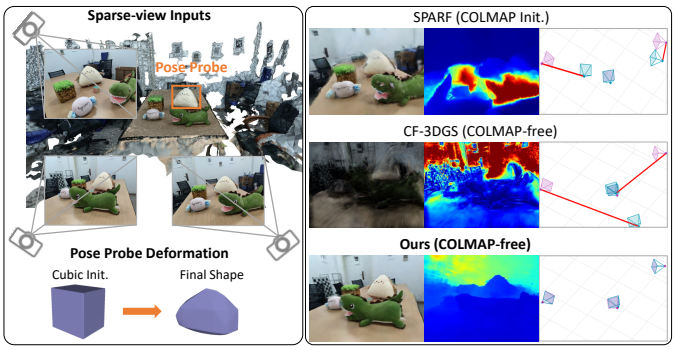

Fig. 1: Our method addresses pose estimation and NeRF-based reconstruction in the challenging few-view settings (only 3 unposed views). Most NeRF-based approaches are initialized from COLMAP poses. However, in sparse regimes, COLMAP often fails to initialize, making it challenging for pose optimization in a state-of-the-art method SPARF [1] to work well. A state-of-the-art COLMAP-free pipeline CF-3DGS [2] also struggles in sparse-view scenarios. We propose to spot generic objects as "pose probes" in the scene (a face-shaped toy in this example), it achieves realistic novel-view renderings and accurately reconstructs geometry using only 3 input images. The precise shapes of pose probes are not required and the proposed DeformNet optimizes them simultaneously.

I. Introduction

As a milestone in the realm of computer vision and graphics, neural radiance fields (NeRFs) offer unprecedented capability of photorealistic rendering of scenes from multi-view posed images. The accuracy of novel-view renderings depends heavily on the precision of input camera poses and the number of input images, limiting its applicability in real-world scenarios. Camera poses of the input views are typically recovered with COLMAP [3] in most prior works. However, we find that if input images are too few and views are too sparse, COLMAP may fail to work due to wide baselines and insufficient feature matches.

To alleviate the reliance on accurate input poses, many studies estimate or refine poses based on various assumptions. Earlier works [4]–[8] predominantly rely on photometric losses to optimize NeRFs and camera poses jointly. For example, NeRFmm [4] focuses on forward-facing scenes where the baseline is relatively small. BARF [5] proposes a coarse-to-fine frequency encoding strategy to facilitate the joint optimization process. GNeRF [6] on the other hand, relies on pose distribution assumptions. However, in sparse-view scenarios, photometric losses alone often prove insufficient for accurate pose estimation due to the under-constrained nature of 3D reconstruction. To address this limitation, methods such as Nope-NeRF [9] and CF-3DGS [2] leverage monocular depth estimation from dense video frames to introduce additional constraints. However, their reliance on dense input frames significantly restricts their applicability in few-view cases. More recently, SPARF [1] and TrackNeRF [1] have advanced pose optimization for few-view settings by utilizing reprojection consistency, marking notable progress in pose-optimized NeRF development. Despite these achievements, they still depend on reasonably pose initialization and cannot operate entirely without prior pose information. Consequently, reconstructing NeRFs in few-view scenarios without any pose priors remains a significant challenge in the field. In this paper, we propose a COLMAP-free approach tailored for few-view inputs, as demonstrated in Fig. 1.

A traditional way to obtain accurate poses is to place a calibration board in the scene. However, calibration boards

All authors are with the School of Computer, National University of Defense Technology, Changsha, 410073, China.

† Corresponding authors: Renjiao Yi and Kai Xu (E-mails: yirenjiao@nudt.edu.cn, kevin.kai.xu@gmail.com).

are not easily accessible in everyday scenes and images. This limitation inspires us to explore the potential of utilizing ubiquitous everyday objects, such as Coke cans, as calibration probes. Such objects are easily found in photos and offer a practical, low-burden alternative. After spotting a probe object, we adopt Grounded-SAM [10] to segment it using text prompts automatically, and a cuboid is used as its shape initialization. The main idea is leveraging everyday objects as pose probes to facilitate the estimation of camera poses. We focus on exploring two main benefits of pose probes: (1) An incremental camera pose optimization strategy addresses the challenge of missing initial poses. New views are added incrementally, with initial poses estimated using the Perspective-n-Point, which leverages the initial probe's geometry and image correspondences. (2) Pose probes establish strong pose constraints, which significantly enhance pose accuracy and, in turn, improve the quality of novel view rendering. We find that most daily objects can be efficiently employed as pose probes (Fig. 10), the method is insensitive to the choice of probe objects.

We introduce a pipeline for NeRF reconstruction from few-view (3 to 6) unposed images. The overall pipeline is shown in Fig. 2, where a dual-branch volume rendering optimization workflow is adopted, targeting the probe object and the entire scene respectively. The object branch employs a hybrid architecture designed for efficient volume rendering. Geometry is represented using a signed distance field (SDF) voxel grid, serving as a template field, combined with an implicit DeformNet to capture deformations. The SDF voxel grid is initialized as a cuboid, representing the initial shape of the pose probe, which is subsequently refined through deformation by the DeformNet. Appearance is represented by a feature grid, and all components are unified through a shallow MLP to enable volume rendering, facilitating the joint optimization of camera poses and object geometry. To enforce learning accurate camera poses and object geometry, the training process incorporates constraints such as multi-view geometric consistency and deformation regularization. Meanwhile, the scene branch is designed to learn a neural representation of the entire scene while refining camera poses. To further enhance convergence in both pose estimation and scene reconstruction, multi-layer feature-metric consistency is introduced as an additional constraint.

The initial camera poses for the first two views are estimated using PnP, leveraging the correspondences of the pose probe between two images and its initial cuboid shape. Subsequent frames are incrementally incorporated during the optimization, also using PnP to estimate initial poses. Poses are further optimized jointly by both branches to get final results. Note that PnP matching requires only several feature matches, working for feature-sparse scenarios, while COLMAP often fails due to insufficient feature matches. As tested in Tab. VIII, even using an identity matrix or very noisy poses (adding 30% noises to PnP poses), the method still gets comparable performance with a slight drop in metrics. In this way, we obtain high-quality novel view synthesis and poses, without any pose priors, even for large-baseline and few-view images. As shown in Fig. 1, aided by the proposed pose probe (the face toy), our method produces realistic novel-view renderings and accurate poses using only three input images, without relying on pose initialization, outperforming both COLMAP-based and COLMAP-free state-of-the-art methods.

The main contributions include:

- We utilize generic objects as pose calibration probes, to tackle the challenging few-view and feature-sparse scenes using only 3 to 6 images, where COLMAP may be inapplicable.
- We propose a hybrid explicit-implicit SDF representation to bridge CAD initialization and implicit deformations efficiently. The whole pipeline is end-to-end differentiable and fully self-supervised.
- We propose a texture-sparse scene dataset, and compare the proposed method with SOTAs across four benchmarks, where our method achieves PSNR improvements of 14.3%, 5.09%, 1.93% and 5.30% in novel view synthesis on average, along with significant enhancements in pose metrics. The proposed method successfully handles sparse-view scenes where COLMAP experiences a 67% initialization failure rate.

II. Related Works

A. Radiance fields with pose optimization

The reliance on high-precision camera poses as input restricts the applicability of NeRFs and 3D Gaussian Splatting [11] (3DGS). Several studies have sought to alleviate this dependency. NeRF-based techniques utilize neural networks to represent the radiance fields and jointly optimize camera parameters, as demonstrated by early approaches [4], [5], [8], [12]. NeRFmm [4] jointly optimizes the radiance field and camera parameters and works on forward-facing scenes. BARF [5] introduces a coarse-to-fine positional encoding strategy, making the joint pose and scene optimization easier. L2G-NeRF [7] integrated a local-to-global registration into BARF to improve anti-noise ability. SCNeRF [8] further optimizes camera distortion and proposes a geometric loss to regularise learned parameters. GARF [12] and SiNeRF [13] employ different activation functions to overcome local minima in optimization. LU-NeRF [14] operates in a local-to-global manner to achieve a final global optimization of camera poses and scenes without pose assumption. CRAYM [15] utilizes the correspondence of camera rays to jointly optimize pose and scene representation. This approach not only produces more realistic renderings but also reconstructs finer geometric details. Additionally, Camp [16] proposes using a proxy problem to compute a whitening transform, which helps refine the initial camera poses. Based on RGB-D video sequences, visual SLAM approaches with neural scene representations [17], [18] significantly improve the scene and pose estimation processes. For instance, NoPe-NeRF [9] adopts monocular depth estimation to learn scene representation without depending on pose priors but it is difficult to handle sparse input images. However, it requires pose initialization and cannot render entire scenes. GC-NeRF [19] establishes the photometric constraints and s explores geometry projection during training. SPARF [1] and

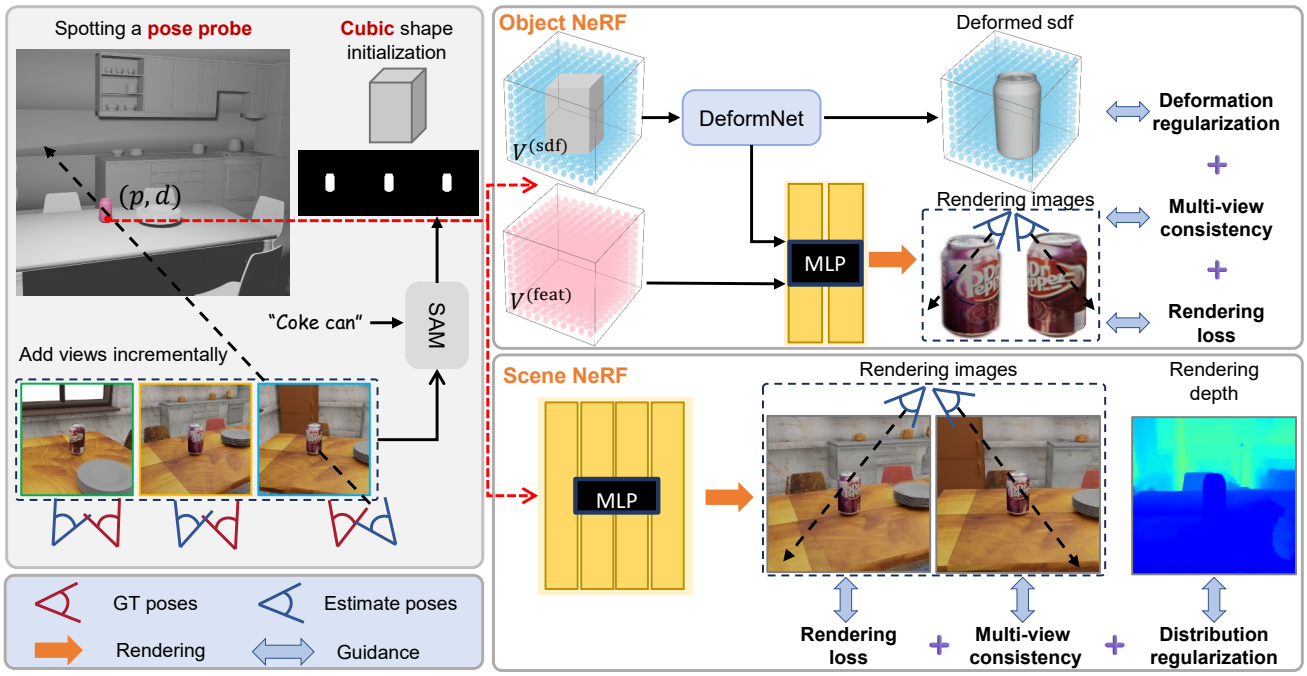

Fig. 2: Method overview. We utilize generic objects as pose probes for few-view inputs. The masks for the pose probe are automatically segmented using Grounded-SAM [10] with text prompts, and its geometry is initialized as a cuboid shape. The pose probe is then leveraged to incrementally estimate the initial poses of input images through a PnP algorithm. Our pipeline employs a dual-branch volume rendering framework for jointly optimizing camera poses and scene geometry. In the object NeRF branch, we adopt a hybrid SDF representation (explicit template SDF grid and implicit DeformNet), to model the object's geometry. This branch enforces robust constraints, such as deformation regularization, multi-view consistency, and rendering loss, to refine poses and object reconstructions. In the scene NeRF branch, we optimize the entire scene within an implicit radiance field while simultaneously refining the camera poses using additional constraints, including rendering loss, multi-view consistency, and distribution regularization.

TrackNeRF [20] address the challenge of NeRFs with sparse-view, wide-baseline input images but require initial camera positions near ground truth, which limits its applicability in real-world scenarios.

3DGS-based approaches utilize explicit 3D Gaussians rather than neural networks and have been explored in various studies. CF-3DGS [2] and COGS [21] leverage monocular depth estimators to assist in registering camera poses. Recent work [22] proposes using an off-the-shelf model [23] to compute initial camera poses and achieve sparse-view and SfM-free optimization. However, 3DGS requires an initialized point cloud, which is often difficult to obtain in unconstrained scenes with sparse viewpoints and unknown poses. Consequently, 3DGS-based methods generally rely on pre-trained vision models [23], [24], significantly increasing complexity.

B. Novel-view synthesis from few views

Novel-view synthesis is one of the fundamental problems in computer vision [25]–[27]. To address the challenge of requiring dense input views, various regularization techniques shine in few-view learning. Some work [28]–[30] utilize depth supervision to avoid overfitting and facilitate better geometry learning. Additionally, appearance regularization [31], geometry regularization [31]–[33] and frequency regularization [1], [34] are introduced to optimize the radiance fields. In addition, AR-NeRF [35] further investigates the inconsistency between the frequency regularization of Positional Encoding and rendering loss, and proposes an adaptive rendering loss regularization to align the frequency relations between them. Some recent works [36]–[40] combine the efficient 3DGS representation and additional geometric constraints(monocular depth estimation [41] or correspondences consistency) to improve the efficiency of novel-view synthesis in sparse-view scenarios. However, these methods assume the availability of ground-truth camera poses, while Structure-from-Motion algorithms often fail with sparse or few inputs, limiting their practical application.

C. Object pose estimation

Object pose estimation is a long-studied problem closely related to camera pose optimization. By leveraging high-fidelity textured CAD models, many approaches [42], [43] match 2D-3D correspondences and then use Perspective-n-Points (PnP) to obtain the poses. CAD model-free pose estimation methods [44], [45] reconstruct the object beforehand, but usually lack good generalization and are difficult to meet the high-precision requirements of NeRF. Other works [46], [47] demonstrate the capability to recover 6D poses from sparse-view observations, but these poses still require refinement during NeRF training. In this paper, we use the consistency of

the pose of the object and the pose of the camera. The poses of the object in the object coordinate system are used as the camera poses to optimize NeRFs.

III. Method

We propose a dual-branch pipeline as illustrated in Fig. 2, which integrates both neural explicit and implicit volume rendering, for which we give some preliminaries in Sec III-A. In the object branch (Sec III-B), we utilize neural volume rendering with a hybrid signed distance field (SDF) to efficiently optimize both camera poses and object representation. In the scene branch (Sec. III-C), the scene representation is learned in an implicit NeRF, while the camera pose is optimized simultaneously. The joint training is described in Sec. III-D.

A. Preliminaries

Explicit volumetric representation. DVGO [48] proposes to optimize a density voxel grid $\boldsymbol{V}^{(\text{density})} \in \mathbb{R}^{1\times N_x\times N_y\times N_z}$ and a feature voxel gird $\boldsymbol{V}^{(\text{feat})} \in \mathbb{R}^{D\times N_x\times N_y\times N_z}$ with a shallow MLP parameterized by Θ, where D is a hyperparameter for feature-space dimension. Given a 3D position $\boldsymbol{p}$ and viewing-direction $\boldsymbol{d}$, the volume density $\boldsymbol{\sigma}$ is estimated by:

$$\boldsymbol{\sigma} = \text{interp}\left(\boldsymbol{p}, \boldsymbol{V}^{(\text{density})}\right), \tag{1}$$

where "interp" denotes trilinear interpolation. The color $\boldsymbol{c}$ is performed by:

$$\boldsymbol{c} = \text{MLP}_\Theta\left(\text{interp}(\boldsymbol{p}, \boldsymbol{V}^{(\text{feat})}), \boldsymbol{p}, \boldsymbol{d}\right). \tag{2}$$

The positional encoding [49] is applied for both $\boldsymbol{p}$ and $\boldsymbol{d}$.

Neural SDF representation. With neural volume rendering, the estimated colors of the image can be presented as:

$$\hat{C} = \sum_{i=1}^{n} w\left(t_i\right)\hat{c}\left(t_i\right), \tag{3}$$

where t_i is the depth of the i th of point sampled along the ray, $w\left(t_i\right)$ and $\hat{c}\left(t_i\right)$ is the weight and the estimated color field for the point at t_i.

$$w\left(t_i\right) = T\left(t_i\right)\alpha\left(t_i\right), T\left(t_i\right) = \sum_{j=1}^{i-1}(1-\alpha\left(t_j\right)), \tag{4}$$

where $T\left(t_i\right)$ is the accumulated transmittance and $\alpha\left(t_i\right)$ is the opacity value. For SDF representations [50]–[52], $\alpha\left(t_i\right)$ is calculated as:

$$\alpha_i = \max\left\{\frac{\Phi_s(sdf(p_i)) - \Phi_s(sdf(p_{i+1}))}{\Phi_s(sdf(p_i))}, 0\right\}. \tag{5}$$

$\Phi_s(x) = (1+e^{-sx})^{-1}$ is the Sigmoid function, in which the parameter s is learnable or manually updated during training. In our method, we also adopt an SDF-based volumetric rendering.

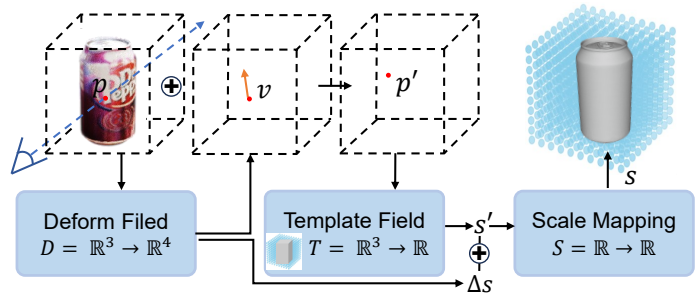

Fig. 3: Overview of the hybrid SDF representation. For a given sampled point $\boldsymbol{p}$ in the input space, the implicit deformation field predicts a deformation vector $\boldsymbol{v}$ and a scalar correction Δs. The point position is first deformed to $\boldsymbol{p}' = \boldsymbol{p} + \boldsymbol{v}$, which is used to query the SDF value s' from the template field. The final SDF value s is computed by a non-linear scale mapping function S to the sum of s' and Δs.

B. Object NeRF with pose estimation

Inspired by the fast convergence of explicit representations [48], [52] while maintaining high-quality rendering, we design a similar volume rendering framework for the object (pose probe) branch. To recover high-fidelity geometry and accurate camera poses, we employ an SDF-based [50], [53] voxel grid for volume rendering. In particular, we propose a hybrid representation combining both explicit and implicit SDF, where each point $\boldsymbol{p}$ is assigned a scalar s:

$$SDF : \boldsymbol{p} \in \mathbb{R}^3 \longrightarrow s \in \mathbb{R} \tag{6}$$

To better utilize the geometry of the object, the gradient at each point is embedded into the color rendering process:

$$\boldsymbol{c} = \text{MLP}_\Theta\left(\text{interp}(\boldsymbol{p}, \boldsymbol{V}^{(\text{feat})}), \boldsymbol{n}, \boldsymbol{p}, \boldsymbol{d}\right). \tag{7}$$

Here, the normal $\boldsymbol{n}$ is computed as the normalized gradient of the SDF, and $\boldsymbol{d}$ represents the viewing direction.

Next, we delve into the hybrid explicit-implicit representation of the object branch. Following this, we introduce how to leverage the pose probe to obtain the initial camera poses for each frame. We then outline strategies for jointly optimizing neural fields and camera poses with the assistance of the pose probe. Note that the goal of the object NeRF is to provide initial camera poses and establish camera pose constraints by modeling the pose probe.

1) Hybrid SDF representation: In the design of a hybrid explicit-implicit SDF generation network, the explicit template field T is a non-learnable voxel grid $\boldsymbol{V}^{(\text{sdf})}$, initialized with the shape of the pose probe, while the implicit deform field D is implemented as MLPs to predict a deformation field and a correction field on top of T, as illustrated in Fig. 3. The voxel grid $\boldsymbol{V}^{(\text{sdf})}$ is initialized with a coarse template (e.g., a cuboid), which we find sufficient for learning detailed geometry and enforcing camera pose constraints. We obtain the SDF values in $\boldsymbol{V}^{(\text{sdf})}$ by calculating the closest distance from each voxel center to the surface and determining whether the point lies inside or outside the object. This process is efficient and takes only a few seconds. The template field T serves as a strong prior, significantly reducing the search space from the

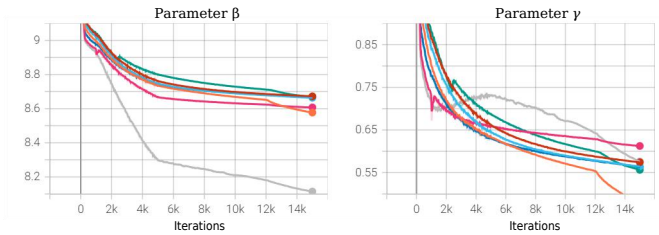

Fig. 4: The adaptive tuning of the training parameters β and γ in the SDF mapping function. These two parameters vary from scene to scene, with different colored curves representing different scenes.

baseline and enabling detailed geometry reconstruction with fewer parameters. We provide an ablation study in Sec. IV-C1 demonstrating that initializing with a template field leads to faster convergence and more accurate geometry compared to learning the SDF field from scratch.

To capture shape details, we employ an implicit deformation field D to refine the coarse SDF. Although optimizing an explicit SDF correction voxel grid on top of the template field T appears more straightforward, it frequently leads to degenerate solutions and geometric artifacts in sparse-view inputs, as discussed in Sec. IV-C5. In contrast, the implicit field inherently provides a smooth and continuous representation, which is well-suited for capturing fine details and complex deformations. Inspired by [54], Our deform field D predicts a deformation vector v and a scalar correction value Δs for each point $\boldsymbol{p}$:

$$D : \boldsymbol{p} \in \mathbb{R}^3 \longrightarrow (v, \Delta s) \in \mathbb{R}^4 \tag{8}$$

The ultimate shape is determined by interpolating at its deformed location within the template field T, further refined by a correction scalar. Therefore, the SDF value of the point $\boldsymbol{p}$ is represented as:

$$\begin{aligned} \text{SDF}(\boldsymbol{p}) &= T(\boldsymbol{p} + D_v(\boldsymbol{p})) + D_{\Delta s}(\boldsymbol{p}) \\ &= \text{interp}\left(\boldsymbol{p} + v, \boldsymbol{V}^{(\text{sdf})}\right) + \Delta s. \end{aligned} \tag{9}$$

The predicted SDF value in our hybrid representation is to estimate volume opacity. But directly using the SDF values in Eqn. 9 is not perfect for volume rendering since the value scale is predefined manually. To this end, we propose a mapping function S with two learnable parameters to scale the original SDF to the scene-customized scale:

$$S(\boldsymbol{p}) = \beta(1/(1 + e^{-\gamma \cdot SDF(\boldsymbol{p})}) - 0.5), \tag{10}$$

where β and γ are trainable parameters to control the scale of SDF voxel grid $\boldsymbol{V}^{(\text{sdf})}$. To ensure that β and γ are always positive for maintaining the original SDF sign, we apply the Softplus activation function to them. The parameters β and γ vary from scene to scene as illustrated in Fig 4. Our hybrid SDF representation merges the advantages of explicit and implicit representations, balancing rapid convergence with detailed modeling.

2) Incremental pose optimization: We employ an incremental pose optimization process, adding a new image is introduced into the training loop at regular intervals. Given the input images and corresponding masks of the pose probe, the first image serves as the reference image, denoted as I. Multiple projection views around the object are sampled to acquire mask images, and the view with the best matching mask is chosen as the initial pose for the first frame. For each newly added frame I_{i+1}, we first compute 2D correspondences with the previous image I_i using SuperPoint [55] and SuperGlue [56] as shown in Fig. 5. The matching pixels in the image I_i cast rays to position the surface of the object leveraging the optimized pose P_i, as detailed in Sec. III-B3. This forms 2D-3D correspondences between the newly added image and the object, enabling PnP with RANSAC to compute the initial pose of image I_{i+1}. Then, the added image views and the radiance field are jointly optimized.

3) Surface positioning with ray-casting: Based on the definition of SDF, surface points constitute the point set defined as $\{\boldsymbol{p} | S(\boldsymbol{p}) = 0\}$. With the explicit SDF voxel grid with shallow DeformNet, the surface points corresponding to image pixels can be efficiently estimated through ray casting, similar to [53], [57]. For a given camera pose $\hat{P}$ and each pixel coordinate $\mathbf{x} \in \mathbb{R}^2$, we can compute its corresponding ray in the world coordinate system. The 3D sampled points along this ray are expressed as $\boldsymbol{p}_i = \boldsymbol{o} + t_i \boldsymbol{v}$, where t_i represents the i-th sampled depth. To determine an occlusion-aware surface point, we identify the smallest index i such that the sign of the SDF value at $\boldsymbol{p}_i$ and $\boldsymbol{p}_{i+1}$ differ:

$$i^* = \text{argmin}\left\{i | S(\boldsymbol{p}_i) \cdot S(\boldsymbol{p}_{i+1}) < 0\right\}. \tag{11}$$

Linear interpolation is applied on line $\boldsymbol{p}_i \boldsymbol{p}_{i+1}$ to obtain the surface point $\mathbf{S}$ associated with x and camera pose $\hat{P}$:

$$\mathbf{S}(\hat{P}, x) = \boldsymbol{o} + \hat{t}\boldsymbol{v}, \hat{t} = \frac{S(\boldsymbol{p}_{i^*})\boldsymbol{p}_{i^*+1} - S(\boldsymbol{p}_{i^*+1})\boldsymbol{p}_{i^*}}{S(\boldsymbol{p}_{i^*}) - S(\boldsymbol{p}_{i^*+1})}. \tag{12}$$

4) Geometric consistency: Recently, SPARF [1] and Track-NeRF [20] propose using reprojection error to enforce geometry and camera poses consistency, achieving remarkable results. Inspired by them, we employ a more direct multi-view projection distance to constrain camera poses as shown in Fig. 5. Formally, given an image pair (I_i, I_j) and matching pixel pairs $(\mathbf{x}, \mathbf{y})$, we first locate the surface points $(\mathbf{S_x}, \mathbf{S_y})$ using ray-casting. 3D surface points are then projected back to the image coordinate to minimize the distance between correspondences. The geometric circle projection distance of pair $(\mathbf{x}, \mathbf{y})$ is defined as:

$$\mathcal{D}(\mathbf{x}, \mathbf{y}) = \rho(\pi(\mathbf{S_x}, \hat{P}_j) - \mathbf{y}) + \rho(\pi(\mathbf{S_y}, \hat{P}_i) - \mathbf{x}), \tag{13}$$

where π means the camera projection function, and ρ denotes Huber loss function. Additionally, based on the prior that rays emitted from feature points should intersect the object, we introduce a regularization term that minimizes the distance between these rays and the surface of the pose probe to refine the camera poses:

$$\mathcal{L}_{\text{dis}}(\boldsymbol{r}, \boldsymbol{o}) = \max(\text{dis}(\boldsymbol{r}, \boldsymbol{o}) - L, 0), \tag{14}$$

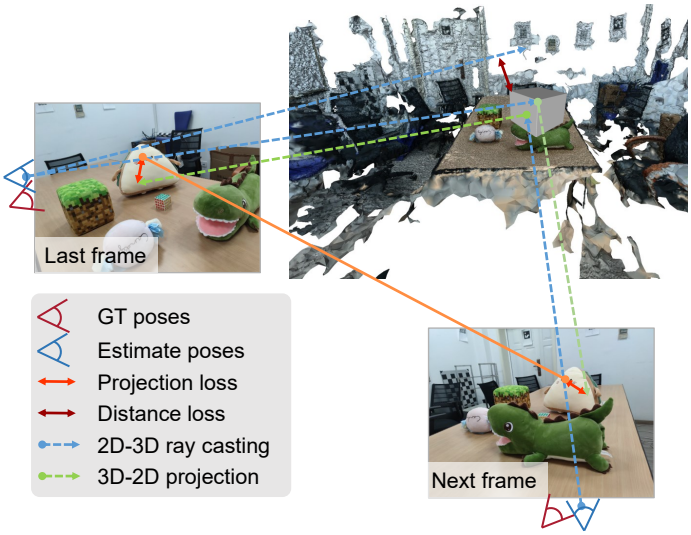

Fig. 5: Illustration of multi-view geometric consistency and ray distance loss. Multi-view geometric consistency ensures accurate alignment of corresponding points across multiple views by minimizing the reprojection error, while the ray distance loss regularizes the minimal distance between camera rays and the surface of the pose probe. Together, these contribute to improved scene reconstruction and camera pose estimation.

where $\text{dis}(\boldsymbol{r}, \boldsymbol{o})$ denotes the shortest distance from the object center $\boldsymbol{o}$ to the ray $\boldsymbol{r}$, and L represents the maximum radius of the object. Finally, our multi-view geometric consistency objective is formulated as:

$$\mathcal{L}_{\text{GeoObj}}(\hat{\mathcal{P}}) = \sum_{(\mathbf{x},\mathbf{y})\in\mathcal{V}} w_{\mathbf{x}}\mathcal{D}(\mathbf{x},\mathbf{y}) + \lambda\mathcal{L}_{\text{dist}}(\boldsymbol{r}_{\boldsymbol{x},\boldsymbol{y}}, \boldsymbol{c}). \quad (15)$$

Here, $w_{\mathbf{x}}$ represents the matching confidence associated with pair $(\mathbf{x}, \mathbf{y})$ and λ is set to 10.

C. Scene NeRF with pose refinement

While training the object NeRF, we simultaneously train a scene NeRF branch. The aim is to learn the scene representation while refining camera poses. To validate the effectiveness of our proposed modules, we employ a baseline NeRF model with coarse-to-fine positional encoding [5]. The projection distance loss (Eqn 13) is also incorporated as a constraint in the scene branch. Furthermore, we adopt two additional constraints to improve the performance.

1) Multi-layer feature-metric consistency: While geometric consistency facilitates rapid convergence in camera pose optimization, mismatches may introduce incorrect supervisory signals, potentially leading to local optimal. Inspired by dense bundle adjustment [58], we introduce a multi-layer feature-metric consistency. This constraint minimizes the feature difference of aligned pixels using cosine similarity. The multi-layer feature-metric associated with pixel $\mathbf{x}$ is formulated as:

$$e_{\mathbf{x}} = \sum_{k=1}^{M} 1 - \cos\left(F_{j,k}(\pi(\mathbf{S}_{\mathbf{x}}, \hat{P}_j)), F_{i,k}(\mathbf{x})\right), \quad (16)$$

where $\mathbb{F} = \{F_{i,k} | i = 1...N, k = 1...M\}$ are the multi-layer image features extracted by the pretrained VGG [59]. Here, N denotes the number of images, and M is the number of layers. Our feature-metric loss is defined as:

$$\mathcal{L}_{\text{Fea}}(\hat{\mathcal{P}}) = \sum_{x\in\mathcal{V}} \gamma_{\mathbf{x}} e_{\mathbf{x}}.$$

A visible mask $\gamma \in [0, 1]$ is applied to filter out out-of-view or occluded points from alternative perspectives. Points whose projected pixels fall outside the image boundary are considered out-of-view, while points with invalid depth values are treated as occluded. To identify occluded pixels, we follow the strategy of SPARF [1], which calculates the cumulative density along a ray to detect occupied regions from other views. This constraint considers more image pixels rather than focusing solely on keypoints in the geometric consistency. In contrast to photometric error, which is sensitive to initialization and increases non-convexity [60], our feature-based consistency loss provides smoother optimization.

2) Compact distribution regularization: We have observed that "background collapse" tends to occur in the training, especially in scenes with few textures. Background collapse is a phenomenon in which distant surfaces tend to gather near the camera [61]. Inspired by Mip-NeRF 360 [61], we adopt a similar regularize to encourage the distribution of density in the radiance field to be compact:

$$\mathcal{L}_{\text{Dist}}(\hat{d}, \mathbf{w}) = \sum_{i,j} w_i w_j \left| \frac{\hat{d}_i + \hat{d}_{i+1}}{2} - \frac{\hat{d}_j + \hat{d}_{j+1}}{2} \right| + \frac{1}{3}\sum_i w_i^2(\hat{d}_{i+1} - \hat{d}_i), \quad (17)$$

where $\hat{d}_i$ is the sampling depth of i-th sampling points and w_i is the alpha compositing.

D. Joint training

The final training objectives consist of all losses for the object NeRF and scene NeRF: $\mathcal{L} = \lambda\mathcal{L}_{\text{Obj}} + \mathcal{L}_{\text{Sce}}$.

1) Object NeRF: To encourage smoother deformation and prevent large shape distortion, we incorporate a deformation regularization on the deformation field and a minimal correction prior [54] for the correction field:

$$\mathcal{L}_{\text{d}} = \sum_{\boldsymbol{p}\in\Omega} \sum_{d\in X,Y,Z} \|\nabla D_v|_d(\boldsymbol{p})\|_2 + \sum_{\boldsymbol{p}\in\Omega} |D_{\Delta s}(\boldsymbol{p})|. \quad (18)$$

Besides, we add an Eikonal term [62] to regularize the the SDF:

$$\mathcal{L}_{\text{r}} = \sum_{\boldsymbol{p}\in\Omega} |\,\|\nabla S(\boldsymbol{p})\|_2 - 1|. \quad (19)$$

$$\mathcal{L}_{\text{Obj}} = \mathcal{L}_{\text{rgb}} + \mathcal{L}_{\text{m}} + \lambda_1\mathcal{L}_{\text{GeoObj}} + \lambda_2\mathcal{L}_{\text{d}} + \lambda_3\mathcal{L}_{\text{r}}, \quad (20)$$

where $\mathcal{L}_{\text{rgb}}$ and $\mathcal{L}_{\text{m}}$ represent photometric l_2 loss and mask l_1 loss respectively. We set λ_1, λ_2, and λ_3 to 0.01, 0.001 and 0.01.

2) Scene NeRF: In the scene training stage, the total loss is:

$$\mathcal{L}_{\text{Sce}} = \mathcal{L}_{\text{rgb}} + \lambda_4\mathcal{L}_{\text{GeoSce}} + \lambda_5\mathcal{L}_{\text{Fea}} + \lambda_6\mathcal{L}_{\text{Dist}}, \quad (21)$$

where λ_4, λ_5, and λ_6 are set to 0.01, 0.001 and 0.001.

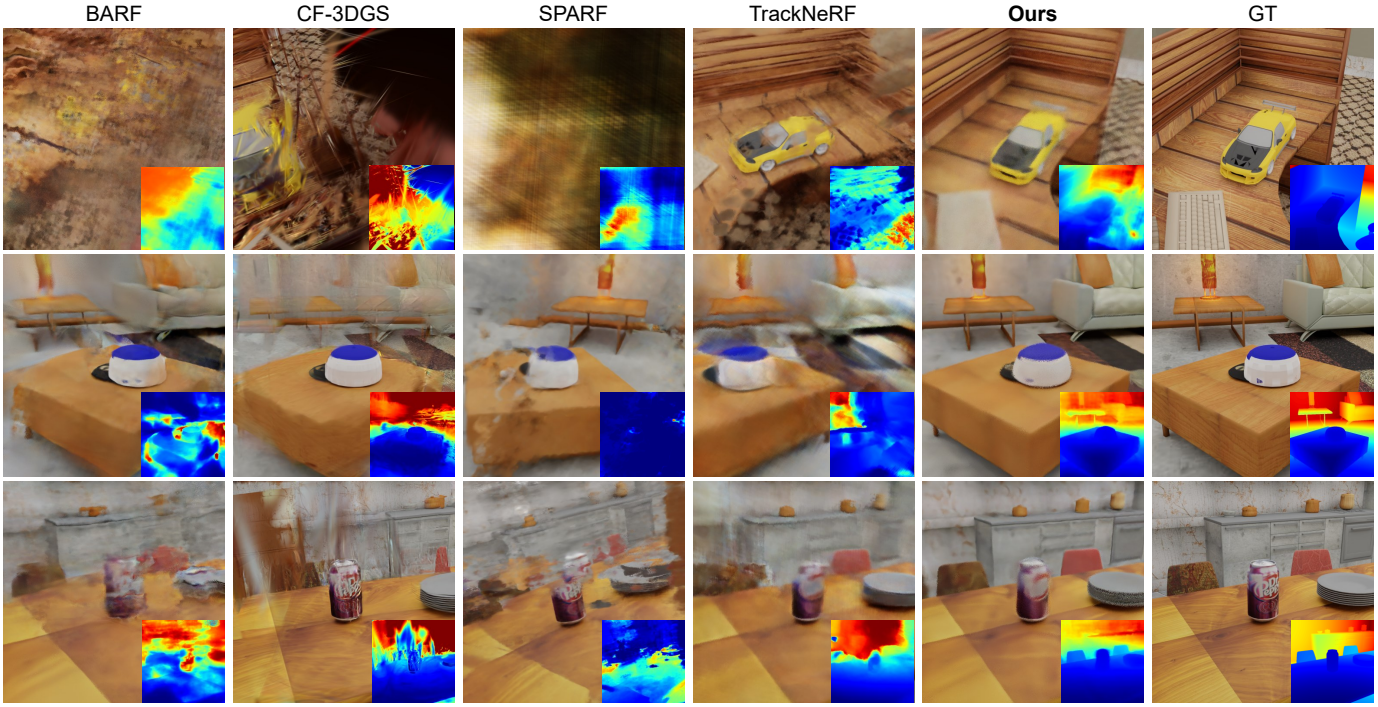

Fig. 6: Qualitative comparison on the ShapeScene dataset. We present novel-view RGB and depth renderings generated by baselines and our approach. The first case uses 3 input views, while the last two cases use 6 input views. Unlike the baselines, which suffer from blurriness and inaccurate scene geometry, our method generates more realistic novel views and reliable depth. We use the central objects in the scene as pose probes.

IV. Experiments

We begin with a description of the experimental settings in Sec. IV-A. In Sec. IV-B, we compare our method with state-of-the-art baselines for camera pose estimation and novel view synthesis in few-view (3∼6) settings across multiple benchmarks. Furthermore, in Sec. IV-C, we present a series of ablation studies to assess the effectiveness of key components and extensively analyze our method. Additional results are available in the supplementary videos.

A. Experimental settings

1) Datasets: We conduct experiments on four datasets: ShapeScene, ToyDesk [63], ,DTU [64] and Replica [65].

ShapeScene is a texture-sparse and synthetic dataset with precise camera poses, providing a challenging benchmark for radiance fields with pose optimization. It is generated using BlenderProc [66] and consists of six scenes rendered jointly from SceneNet [67] and ShapeNet [68]. To demonstrate the generality of our approach, we select a diverse set of scenes and objects: two bedroom scenes, two kitchen scenes, and two office scenes from SceneNet, along with two cans, a car, a keyboard, a hat, and a sofa from ShapeNet. Each scene includes 100 RGB images with a resolution of 512×512, along with corresponding mask images, captured around the ShapeNet object at 360°. To create a sparse-view and wide-baseline scenario, we subsample every k^{th} frame and randomly select a set of consecutive training images from this subsampled set.

ToyDesk is introduced by Object-NeRF [63] and comprises two sets of posed images, each with a resolution of 480×640. The scenes depict a table with various toys arranged, captured from 360° viewpoints. This setup aligns well with the design of our method, and we utilize different toys on the desk as pose probes. We subsample every k^{th} frame and a triplet of consecutive training images.

Replica consists of videos capturing room-scale indoor scenes. For evaluation, we select two room scenes and two office scenes. Frames are subsampled by selecting every k^{th} frame, following a protocol similar to that of SPARF [1], to determine training and testing images. DTU is composed of object-level scenes with wide-baseline views covering a half hemisphere, we select 8 scans that feature both foreground objects and backgrounds for our test set. The training and testing sets are separated according to the dataset splitting protocol outlined in SPARF [1]. In all experiments, our method and the comparison method use the same data set, and the comparison method uses the default training parameters.

2) Metrics: For camera pose evaluation, we report the average rotation and translation errors as pose metrics [1] after aligning the optimized poses with the ground truth. For novel view synthesis, we report the PSNR, SSIM [69], LPIPS [70] (with AlexNet [71]). We also present the Average metric (the geometric mean of $10^{-\text{PSNR}/10}$, $\sqrt{1-\text{SSIM}}$, and LPIPS) following [34].

3) Implementation details: The segmentation masks of pose probes from the input images are automatically generated using Grounded-SAM [10], [72] with text prompts. In the object NeRF, the DeformNet is an MLP with three hidden layers, each containing 128 units. The SDF mapping parameters are

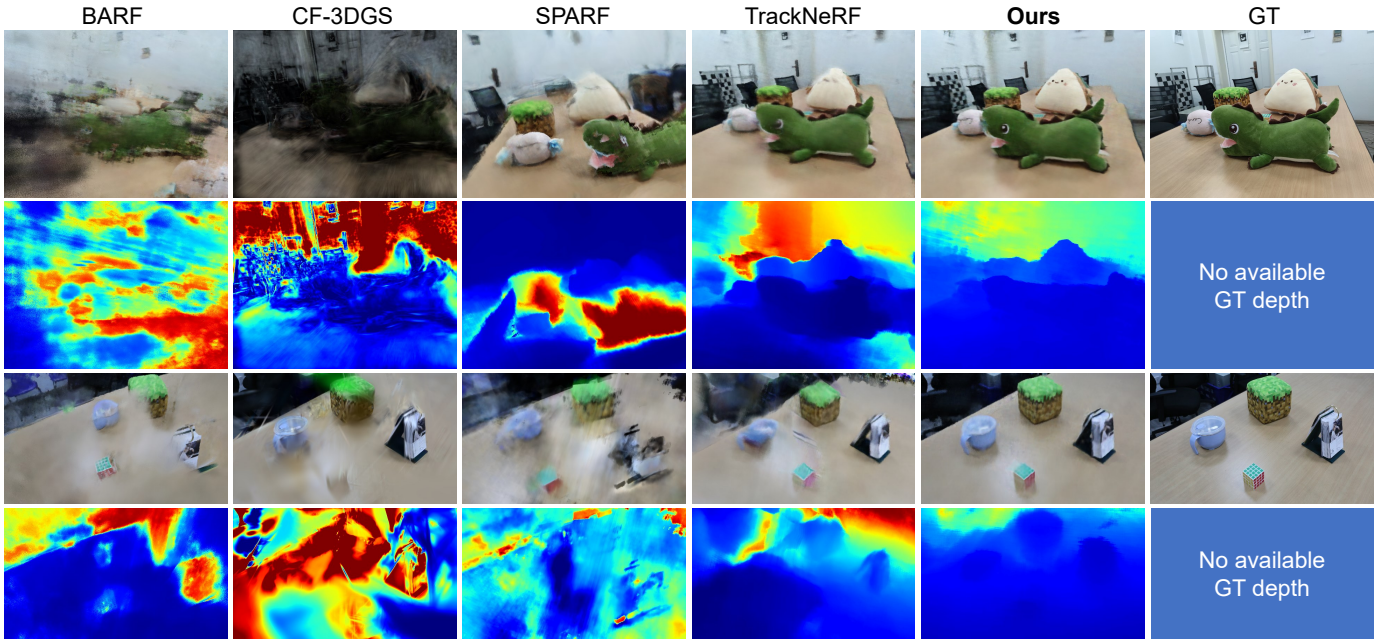

Fig. 7: Qualitative comparison on the ToyDesk dataset. We show novel-view renderings of the baselines and our method with 3 input views. Compared to the baselines, our method produces more detailed and realistic renderings. We use the face-shaped toy (first row) and the magic cube (second row) as pose probes.

TABLE I: Quantitative evaluations on the ShapeScene. Rotation error (Rot.) is reported in degrees, while translation error (Trans.) is the ground truth scale multiplied by 100.

	Rot. ↓		Trans. ↓		PSNR ↑		SSIM ↑		LPIPS ↓		Average ↓	
	3-view	6-view	3-view	6-view	3-view	6-view	3-view	6-view	3-view	6-view	3-view	6-view
CF-3DGS [2]	56.10	35.69	27.32	20.81	16.74	18.31	0.49	0.65	0.52	0.47	0.20	0.16
SCNeRF [8]	10.95	9.88	7.72	14.65	16.39	16.74	0.51	0.53	0.58	0.55	0.21	0.20
BARF [5]	8.25	13.15	10.53	10.02	17.95	18.97	0.56	0.58	0.65	0.64	0.19	0.17
SPARF [1]	6.41	14.48	6.27	21.45	18.29	16.57	0.65	0.56	0.45	0.48	0.16	0.19
TrackNeRF [20]	2.67	3.42	5.48	7.11	18.93	22.57	0.66	0.69	0.41	0.33	0.15	0.10
Ours	**0.72**	**0.70**	**1.89**	**1.06**	**23.11**	**26.08**	**0.68**	**0.79**	**0.38**	**0.25**	**0.10**	**0.07**

initialized as $\beta = 10$ and $\gamma = 2$. Both the SDF voxel grid $V^{(\text{sdf})}$ and feature voxel grid $V^{(\text{fea})}$ have dimensions of 96^3, and the step size for sampling points is 1.5 times the voxel size. The shallow MLP has four hidden layers, each with 128 units, and the feature voxel grid has 12 channels. Coarse-to-fine positional encoding [5] is applied, with frequency widths ranging from 0.5 to 1 for object NeRF and 0.4 to 0.7 for scene NeRF. The new frame is added every 2k iterations. Given that too few images may not suffice to train the deformation network effectively, we fix the parameters of the deformation network while adding images. Once all images are incorporated, the entire network is optimized synchronously. We use Adam with an exponential learning rate decaying from 10^{-3} to 10^{-4} for optimizing the camera poses. The learning rates of the feature voxel grid and shallow MLP are set to 0.1 and 0.001. The learning of β and γ in the mapping function is 0.01. The object NeRF is trained for 15K iterations and the scene NeRF for 66K iterations, using a batch size of 1024 pixel rays. Camera poses are optimized only during the first 30% of training. The entire process takes approximately 6 hours on a single NVIDIA 3090 GPU.

TABLE II: Quantitative comparison on the ShapeScene (3 views). We present quantitative results optimized from GT-noisy poses. Rot. denotes errors in degrees and Trans. is the ground truth scale multiplied by 100.

	Rot. ↓	Trans. ↓	PSNR ↑	SSIM ↑	LPIPS ↓	Average ↓
CF-3DGS [2]	30.74	27.16	17.13	0.52	0.50	0.19
SCNeRF [8]	3.59	6.49	19.65	0.61	0.43	0.14
BARF [5]	10.66	27.43	16.41	0.52	0.66	0.22
SPARF [1]	6.04	8.65	21.21	0.64	0.41	0.12
TrackNeRF [20]	2.04	6.27	21.88	0.65	0.40	0.11
Ours	**1.31**	**1.78**	**23.06**	**0.68**	**0.37**	**0.10**

B. Comparison with State-of-the-arts

We compare our method against state-of-the-art pose-free methods, including BARF [5], SCNeRF [8], SPARF [1], TrackNeRF [20], as well as CF-3DGS [2].

1) Results on ShapeScene: We evaluate our method and baseline approaches using 3 and 6 input views, respectively. To ensure a fair comparison, we use camera poses derived through PnP in our method as initial poses for baselines, as these poses provide better registration than identity poses. Consequently, we also adopt this initialization method by default in subsequent experiments. The initial poses exhibit average rotation and translation errors of approximately 35°

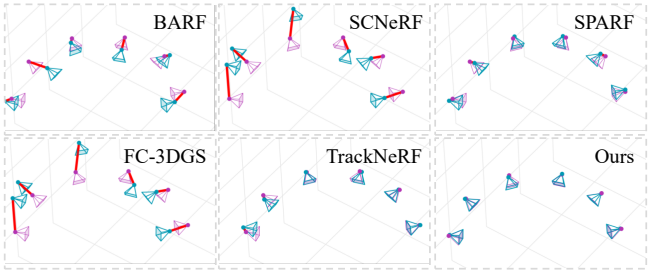

Fig. 8: Qualitative comparison for camera pose estimation. We display the alignment of the optimized poses (in blue) with the ground truth poses (in pink), better viewed when zoomed in.

TABLE III: Quantitative comparison on the ToyDesk (3 views). Rot. denotes errors in degrees and Trans. is the ground truth scale multiplied by 100.

	Rot. ↓	Trans. ↓	PSNR ↑	SSIM ↑	LPIPS ↓	Average ↓
CF-3DGS [2]	53.59	21.66	12.89	0.59	0.73	0.29
SCNeRF [8]	14.64	17.86	13.88	0.59	0.71	0.26
BARF [5]	20.38	19.12	13.17	0.57	0.76	0.29
SPARF [1]	7.71	8.69	15.29	0.62	0.66	0.23
TrackNeRF [20]	0.40	0.65	18.46	0.69	0.49	0.15
Ours	**0.29**	**0.24**	**19.40**	**0.71**	**0.43**	**0.14**

and 70 units, respectively. As shown in Tab. I and Fig. 6, we observe that most baseline approaches fail to accurately register poses and generate poor novel views, as they rely on good initial poses or dense input views. In Fig. 8, we present optimized poses of one scene. To further validate the robustness of our method, we experiment akin to SPARF, adding 20% additive Gaussian noise to the ground truth poses as initial estimates. The perturbed camera poses have an average rotation and translation error of around 20° and 50 units, respectively. Quantitative results are shown in Tab. II. Both BARF and CF-3DGS face persistent challenges in optimizing camera poses, leading to subpar rendering quality. The geometric projection losses employed by SCNeRF, SPARF, and TrackNeRF contribute to the improvement of camera pose estimation. However, they still face challenges in accurately recovering the precise poses. In contrast, our method achieves more accurate pose estimation and more realistic renderings, both from scratch and noisy poses, resulting in higher-quality novel views.

TABLE IV: Quantitative comparison on the DTU (3 views). Rot. is in degrees and Trans. is the ground truth scale multiplied by 100.

	Rot. ↓	Trans. ↓	PSNR ↑	SSIM ↑	LPIPS ↓	Average ↓
CF-3DGS [20]	20.61	22.45	10.84	0.39	0.53	0.32
SCNeRF [8]	11.63	19.13	12.62	0.45	0.57	0.28
BARF [5]	15.37	45.13	10.08	0.39	0.60	0.35
SPARF [1]	3.46	6.48	16.79	0.64	0.30	0.16
TrackNeRF [20]	1.83	4.07	17.58	0.68	**0.26**	0.14
Ours	**1.27**	**3.82**	**17.92**	**0.69**	**0.26**	**0.13**

TABLE V: Quantitative comparison on the Replica (3 views). Rot. denotes errors in degrees and Trans. is the ground truth scale multiplied by 100.

	Rot. ↓	Trans. ↓	PSNR ↑	SSIM ↑	LPIPS ↓	Average ↓
CF-3DGS [2]	13.09	19.7	14.84	0.65	0.49	0.21
SCNeRF [8]	3.91	8.25	18.58	0.68	0.37	0.14
BARF [5]	5.94	22.74	15.17	0.66	0.42	0.20
SPARF [1]	3.25	6.39	22.18	0.76	0.30	0.10
TrackNeRF [20]	2.27	3.19	23.79	0.81	0.25	0.07
Ours	**0.38**	**1.05**	**25.05**	**0.85**	**0.17**	**0.06**

2) Results on ToyDesk: Table III presents the quantitative results on the ToyDesk dataset using three input images. To ensure consistency in the evaluation, the initial camera poses for all baselines are derived from PnP using pose probes. These initial poses have average rotation and translation errors of approximately 11.8° and 9.3, respectively. Notably, CF-3DGS, SCNeRF, and BARF fail to register the camera poses effectively. TrackNeRF performs better than SPARF, recovering more accurate camera poses from highly noisy initial estimates. The visual results are illustrated in Fig. 7, where our method achieves lower camera pose errors and improved rendering quality. These improvements can be attributed to two critical factors: the strong geometric constraints provided by pose probes in the object branch and the global multilayer feature-metric consistency enforced by the scene branch.

3) Results on DTU and replica: We test the DTU and replica datasets with 3 input views and compare our method with state-of-the-art techniques. The PnP camera poses are used as the initial poses for baselines to ensure a fair comparison. The visual results are presented in Fig. 9, the quantitative results are presented in Tab. IV and Tab. V, our method performs better in pose estimation and novel-view synthesis. All baselines suffer from blurriness and inaccurate scene geometry as they rely on strong pose initialization assumptions, while our approach produces closer results to GT thanks to the pose probe constraint.

C. Ablations and analysis

In this section, we conduct ablation studies and analyze the robustness of our approach. The ToyDesk dataset, featuring daily scenes and multiple objects as pose probes, is chosen as the primary dataset for our ablation experiments.

1) Effectiveness of proposed components: As shown in Tab. VI, we evaluate the effectiveness of key modules by conducting ablation studies using three input views on the ToyDesk dataset.

- We establish 2D-3D correspondences between the new image and the 3D model of the pose probe to calculate the initial pose. However, as additional images are added, the errors in camera pose estimated by PnP accumulate, leading to poor initial pose estimates. To mitigate this issue, we propose an incremental pose optimization strategy that calculates the initial poses of new frames based on the previously optimized poses. Omitting this strategy results in a substantial drop in model performance. To provide an intuitive demonstration of this strategy, Fig. 11 illustrates the pose error curves, comparing results with and without incremental optimization. With incremental optimization, camera poses converge faster and achieve more accurate alignment, even with varying input view counts (3, 6, and 9 views).
- In the scene branch, we employ multi-layer feature consistency (Eqn. 16), and density weighting to achieve a compact distribution (Eqn. 17). The former enhances the

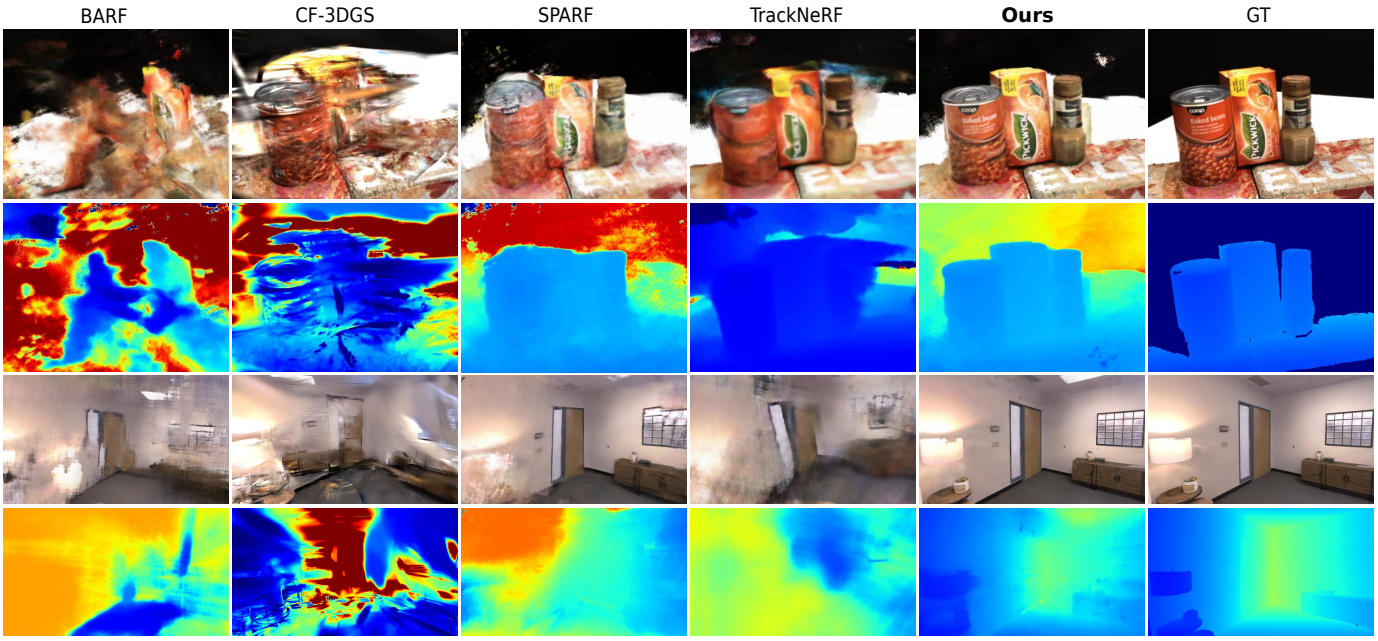

Fig. 9: Qualitative comparison on DTU and Replica dataset. We show novel-view RGB and depth renderings with 3 input views. Our method renders clearer details and fewer artifacts compared to other pose-free baselines. In these two examples, we use a coffee can and windows as pose probes.

TABLE VI: Effect of key modules. We evaluate the impact of different modules by individually disabling them on the ToyDesk dataset. Rot. is in degrees and Trans. is the ground truth scale multiplied by 100.

	Rot. ↓	Trans. ↓	PSNR ↑	SSIM ↑	LPIPS ↓	Average ↓	Times (hrs)
w/o Incre.	4.62	6.03	16.39	0.66	0.60	0.20	6.1
w/o $\mathcal{L}_{\text{Fea}}$	0.43	0.83	18.41	0.69	0.45	0.15	5.1
w/o $\mathcal{L}_{\text{Dist}}$	0.32	0.36	19.28	0.71	0.44	0.14	5.8
w/o $\mathcal{L}_{\text{GeoDist}}$	0.56	0.62	19.02	0.70	0.44	0.14	6.1
w/o $\mathcal{L}_{\text{GeoSce}}$	2.53	5.92	17.14	0.61	0.51	0.18	5.6
w/o $\mathcal{L}_{\text{GeoBoth}}$	17.43	15.73	14.58	0.59	0.73	0.25	5.3
w/o DeformNet	2.14	3.56	17.48	0.62	0.51	0.17	5.7
Full Model	**0.29**	**0.24**	**19.40**	**0.71**	**0.43**	**0.14**	6.1

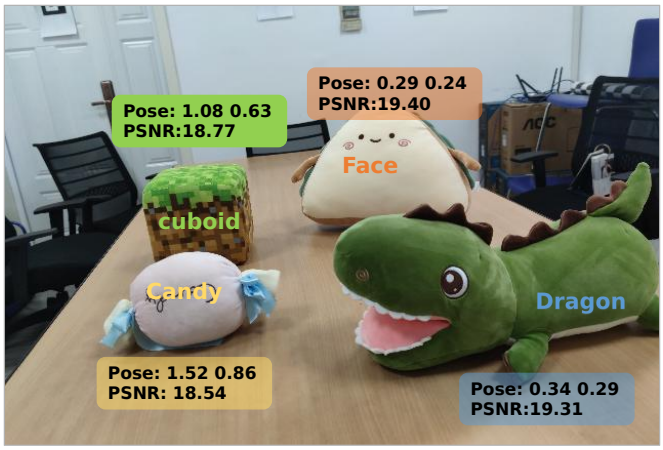

Fig. 10: Evaluation on one scene of ToyDesk with different pose probes. We use the Candy, Face, and Dragon toys in the scene as pose probes, respectively.

registration of camera poses, while the latter facilitates producing higher-quality images with minimal impact on pose optimization.

- The geometric consistency loss (Eqn. 15) plays a crucial role in guiding camera pose optimization. As shown in Tab. VI, the geometric consistency terms in the object branch ($\mathcal{L}_{\text{GeoObj}}$) and in the scene branch ($\mathcal{L}_{\text{GeoScn}}$) both contribute to learning better camera poses. Combining two terms ($\mathcal{L}_{\text{GeoBoth}}$) leads to the highest camera pose accuracy. Omitting these constraints results in a noticeable decline in performance, as inaccurate poses degrade the quality of novel view synthesis.
- DeformNet plays a crucial role in our framework by refining the shape of probe objects and enhancing geometric constraints. This refinement enables more accurate camera pose estimation, resulting in higher-quality novel view synthesis.
- The last column of Tab. VI presents the training time for our method and its ablation studies. Our method requires approximately 6 hours per scene, whereas SPARF and TackNeRF typically take about 10 hours.

2) Impact of different pose probes: To investigate the insensitivity to different pose probes, we utilize a scene from ToyDesk containing multiple partially observed objects. Four

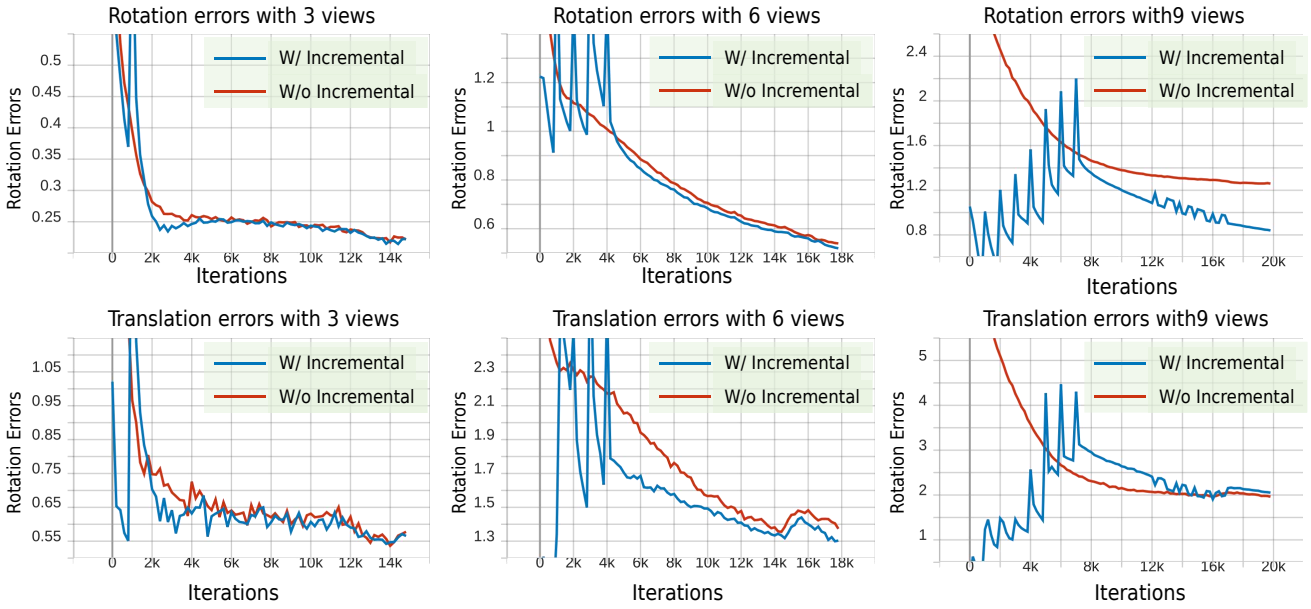

Fig. 11: Rotation and translation errors with or without incremental pose optimization. The blue curve (**Ours**) represents the inclusion of incremental pose optimization, and the red curve indicates that incremental pose optimization is disabled. It is observed that incremental pose optimization converges faster and eventually to a better solution.

toys in the scene are alternately used as pose probes, with all shapes initialized as cuboids. The optimized pose errors and average PSNR values for novel view synthesis are reported in Fig. 10, showing that all pose probes perform effectively.

3) Robustness matching pairs and on initial poses: We compare the robustness of COLMAP [3] and our PnP method by categorizing the data into sparse (3 views) and dense (6 views) splits, using ShapeScene as the dataset for this evaluation. As shown in Tab. VII, the state-of-the-art COLMAP with SuperPoint and SuperGlue (COLMAP-SP-SG) frequently fails in the sparse view split due to insufficient feature pairs for pose initialization. Unlike the SfM pipeline, PnP eliminates the need for the reconstruction process to recover camera poses, relying on fewer features. Our results demonstrate that the proposed method remains effective even when using only half of the matching pairs, highlighting its reduced dependency on pose matching compared to COLMAP. PnP operates reliably with significantly fewer feature pairs, making it suitable for both sparse and dense view settings. It is worth mentioning that the COLMAP poses are further refined using SPARF [1]. Although our method employs PnP to compute the initial poses of new frames, it is not strictly necessary. PnP initialization primarily accelerates pose convergence by providing a more accurate starting point. To validate this, we conducted experiments with 3 input views using various pose initialization strategies, as shown in Tab. VIII. Our method achieves comparable performance when using the previous frame's pose as initialization (identical poses) and remains robust even with substantially noisy poses.

4) Robustness when mask noises exist: In our pipeline, Grounded-SAM [10], [72] is employed with text prompts to generate masks for the object branch, which inevitably contain noise. To evaluate robustness, we performed ablation studies by introducing noise to the masks, as well as dilating

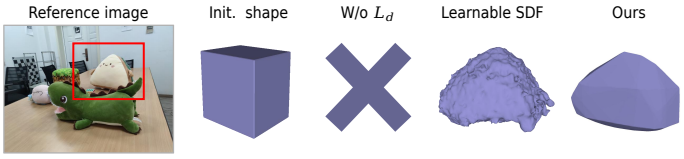

Fig. 12: The impact of different strategies on the object shape is demonstrated. The third column illustrates the shape of removing the deformation regularization loss, while the fourth column shows the result of directly optimizing the SDF grid instead of utilizing a DeformNet.

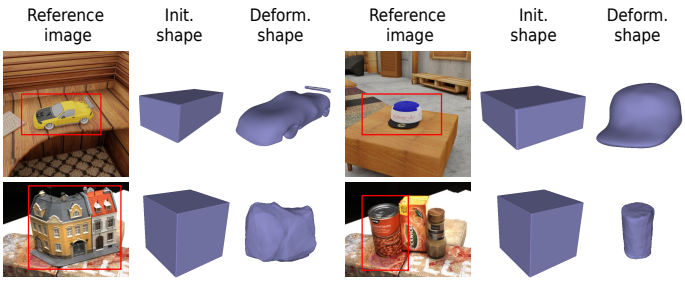

Fig. 13: We present the initial and deformed shapes of the pose probe using the ShapeScene and DTU datasets. The first row corresponds to six input views, while the second row corresponds to three input views. The pose probe within the scene is highlighted by a red box.

and eroding them by 16%, as detailed in Tab. IX. The results demonstrate that our method exhibits good resilience to mask noise, maintaining comparable performance despite these perturbations.

5) Object reconstruction: Although our method does not focus on the reconstruction quality of the probe probes, we

TABLE VII: Performance of COLMAP-based methods and ours. SR represents the success rate of recovering all camera poses, while matches denote the number of matching pairs. "Ours-50%" indicates that only 50% of the matches are used.

Pose init.	Sparse views				Dense views			
	Rot. ↓	Trans. ↓	SR ↑	Matches	Rot. ↓	Trans. ↓	SR ↑	Matches
COLMAP [3]	-	-	0.0%	202	3.38	8.82	83%	2271
COLAMP-SP-SG [55], [56]	10.24	11.61	33%	499	13.58	2.32	100%	3208
Ours-50%	1.97	2.72	100%	137	1.48	2.91	100%	392
Ours	**0.72**	**1.89**	100%	274	**0.70**	**1.06**	100%	783

TABLE VIII: Performance of different pose initialization strategies on ShapeScene dataset (3 views).

Pose init.	Rot. ↓	Trans. ↓	PSNR ↑	SSIM ↑	LPIPS ↓	Average ↓
Identical	1.11	3.15	22.82	0.67	0.38	0.104
30% noise	2.84	7.16	22.25	0.63	0.46	0.119
25% noise	0.81	1.82	22.91	0.67	0.40	0.105
15% noise	0.80	2.30	22.59	0.66	0.39	0.108
PnP	**0.72**	**1.89**	**23.11**	**0.68**	**0.38**	**0.102**

TABLE IX: The effect on Performance with noisy masks on ToyDesk dataset with 3 input views.

Method	Rot. ↓	Trans. ↓	PSNR ↑	SSIM ↑	LPIPS ↓	Average ↓
mask Erosion	0.82	0.73	18.51	0.70	0.44	0.15
mask Dilation	0.35	0.41	19.15	0.71	0.44	0.15
SAM mask	**0.29**	**0.24**	**19.40**	**0.71**	**0.43**	0.14

showcase the geometry of the objects after the deformation network to better understand our approach. The deformation regularization (Eq.18) serves as a crucial constraint for DeformNet. Without this regularization, the shape of the probe object collapses, as the SDF field becomes entirely negative, leading to an empty shape. Another approach to refine the object's shape is directly learning the SDF voxel grid, similar to Voxurf [52]. However, under sparse-view settings, this method often results in significant artifacts in the reconstructed shape. In contrast, the implicit DeformNet offers a more stable and smoother shape. As shown in Fig. 13, it can be observed that even with few input views and a limited number of optimization steps, our object branch achieves a reasonable geometry. Additionally, we conduct experiments comparing our method to NeRS [73], which is specifically designed for object deformation learning. As shown in Fig. 14, using the same dataset and initialization as NeRS, our method effectively handles non-convex objects and reconstructs more detailed structures.

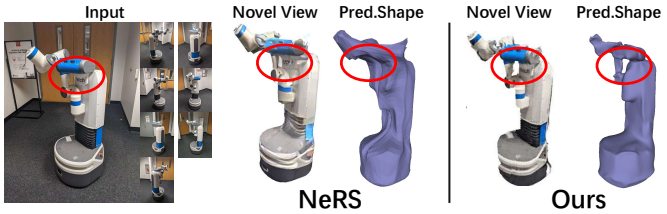

Fig. 14: Compared to NeRS, our method produces more detailed geometry and better novel view synthesis.

D. Failure cases

Our approach relies on extracting correspondences from the multi-view images of the pose probe. However, as illustrated in Fig. 15, if the images of the pose probe contain too few features, resulting in an insufficient number of reliable correspondences, it results in an inability to compute the initial pose using PnP.

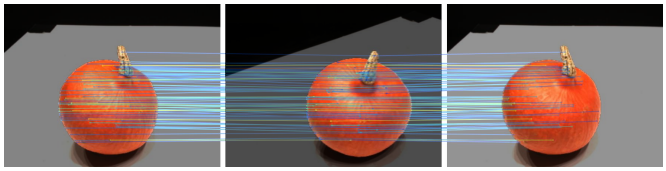

Fig. 15: A failure case for our method occurs when the pose probe has low texture and symmetry, leading to many false matches.

V. Conclusion

We propose PoseProbe, a novel pipeline that leverages generic objects as camera pose probes for joint pose-NeRF training, tailored for challenging scenarios of few-view and large-baseline, where COLMAP is infeasible. By utilizing a hybrid SDF representation of the pose probe, we incrementally acquire initial camera poses, which are subsequently refined through joint optimization with object NeRF and scene NeRF. Multi-view geometry consistency and multi-layer feature consistency are explored to enable the accurate joint optimization of NeRF and camera poses. Our method achieves state-of-the-art performance in pose estimation and novel view synthesis across multiple challenging datasets. However, it may be limited to scenarios where calibration objects are present in all input images. Additionally, as our approach relies on 2D correspondences to initialize and refine poses, it may struggle with featureless objects, such as texture-less spheres.

References

[1] P. Truong, M.-J. Rakotosaona, F. Manhardt, and F. Tombari, "Sparf: Neural radiance fields from sparse and noisy poses," in *Proceedings of the IEEE/CVF Conference on Computer Vision and Pattern Recognition*, 2023, pp. 4190–4200.

[2] Y. Fu, S. Liu, A. Kulkarni, J. Kautz, A. A. Efros, and X. Wang, "Colmap-free 3d gaussian splatting," in *Proceedings of the IEEE/CVF Conference on Computer Vision and Pattern Recognition (CVPR)*, June 2024, pp. 20 796–20 805.

[3] J. L. Schönberger and J.-M. Frahm, "Structure-from-motion revisited," in *2016 IEEE Conference on Computer Vision and Pattern Recognition (CVPR)*, 2016, pp. 4104–4113.

[4] Z. Wang, S. Wu, W. Xie, M. Chen, and V. A. Prisacariu, "NeRF−−: Neural radiance fields without known camera parameters," *arXiv preprint arXiv:2102.07064*, 2021.

[5] C.-H. Lin, W.-C. Ma, A. Torralba, and S. Lucey, "BARF: Bundle-adjusting neural radiance fields," in *ECCV*, 2022.

[6] Q. Meng, A. Chen, H. Luo, M. Wu, H. Su, L. Xu, X. He, and J. Yu, "GNeRF: GAN-based Neural Radiance Field without Posed Camera," in *ICCV*, 2021.

[7] Y. Chen, X. Chen, X. Wang, Q. Zhang, Y. Guo, Y. Shan, and F. Wang, "Local-to-global registration for bundle-adjusting neural radiance fields," in *Proceedings of the IEEE/CVF Conference on Computer Vision and Pattern Recognition*, 2023, pp. 8264–8273.

[8] Y. Jeong, S. Ahn, C. Choy, A. Anandkumar, M. Cho, and J. Park, "Self-calibrating neural radiance fields," in *Proceedings of the IEEE/CVF International Conference on Computer Vision*, 2021, pp. 5846–5854.

[9] W. Bian, Z. Wang, K. Li, J.-W. Bian, and V. A. Prisacariu, "Nope-nerf: Optimising neural radiance field with no pose prior," in *Proceedings of the IEEE/CVF Conference on Computer Vision and Pattern Recognition*, 2023, pp. 4160–4169.

[10] T. Ren, S. Liu, A. Zeng, J. Lin, K. Li, H. Cao, J. Chen, X. Huang, Y. Chen, F. Yan, Z. Zeng, H. Zhang, F. Li, J. Yang, H. Li, Q. Jiang, and L. Zhang, "Grounded sam: Assembling open-world models for diverse visual tasks," 2024.

[11] B. Kerbl, G. Kopanas, T. Leimkühler, and G. Drettakis, "3d gaussian splatting for real-time radiance field rendering." *ACM Trans. Graph.*, vol. 42, no. 4, pp. 139–1, 2023.

[12] S.-F. Chng, S. Ramasinghe, J. Sherrah, and S. Lucey, "GARF: Gaussian activated radiance fields for high fidelity reconstruction and pose estimation," in *ICCV*, 2021.

[13] Y. Xia, H. Tang, R. Timofte, and L. Van Gool, "Sinerf: Sinusoidal neural radiance fields for joint pose estimation and scene reconstruction," *arXiv preprint arXiv:2210.04553*, 2022.

[14] Z. Cheng, C. Esteves, V. Jampani, A. Kar, S. Maji, and A. Makadia, "Lu-nerf: Scene and pose estimation by synchronizing local unposed nerfs," *arXiv preprint arXiv:2306.05410*, 2023.

[15] L. Lin, W. Wu, C.-W. Fu, H. Zhan, and H. Huang, "Craym: Neural field optimization via camera ray matching," in *NeurIPS*, 2024.

[16] K. Park, P. Henzler, B. Mildenhall, J. T. Barron, and R. Martin-Brualla, "Camp: Camera preconditioning for neural radiance fields," *ACM Trans. Graph.*, vol. 42, no. 6, dec 2023. [Online]. Available: https://doi.org/10.1145/3618321

[17] A. Rosinol, J. J. Leonard, and L. Carlone, "Nerf-slam: Real-time dense monocular slam with neural radiance fields," *arXiv preprint arXiv:2210.13641*, 2022.

[18] Z. Zhu, S. Peng, V. Larsson, W. Xu, H. Bao, Z. Cui, M. R. Oswald, and M. Pollefeys, "Nice-slam: Neural implicit scalable encoding for slam," in *CVPR*, 2022.

[19] Q. Zhang, C. Huang, Q. Zhang, N. Li, and W. Feng, "Learning geometry consistent neural radiance fields from sparse and unposed views," in *Proceedings of the 32nd ACM International Conference on Multimedia*, 2024, pp. 8508–8517.

[20] J. Mai, W. Zhu, S. Rojas, J. Zarzar, A. Hamdi, G. Qian, B. Li, S. Giancola, and B. Ghanem, "Tracknerf: Bundle adjusting nerf from sparse and noisy views via feature tracks," in *Computer Vision – ECCV 2024*, A. Leonardis, E. Ricci, S. Roth, O. Russakovsky, T. Sattler, and G. Varol, Eds. Cham: Springer Nature Switzerland, 2025, pp. 470–489.

[21] K. Jiang, Y. Fu, M. Varma T, Y. Belhe, X. Wang, H. Su, and R. Ramamoorthi, "A construct-optimize approach to sparse view synthesis without camera pose," *SIGGRAPH*, 2024.

[22] Z. Fan, W. Cong, K. Wen, K. Wang, J. Zhang, X. Ding, D. Xu, B. Ivanovic, M. Pavone, G. Pavlakos *et al.*, "Instantsplat: Unbounded sparse-view pose-free gaussian splatting in 40 seconds," *arXiv preprint arXiv:2403.20309*, 2024.

[23] S. Wang, V. Leroy, Y. Cabon, B. Chidlovskii, and J. Revaud, "Dust3r: Geometric 3d vision made easy," in *CVPR*, 2024.

[24] R. Ranftl, K. Lasinger, D. Hafner, K. Schindler, and V. Koltun, "Towards robust monocular depth estimation: Mixing datasets for zero-shot cross-dataset transfer," *IEEE Transactions on Pattern Analysis and Machine Intelligence (TPAMI)*, 2020.

[25] B. Liu, B. Peng, Z. Zhang, Q. Huang, N. Ling, and J. Lei, "Unsupervised single-view synthesis network via style guidance and prior distillation," *IEEE Transactions on Circuits and Systems for Video Technology*, 2023.

[26] Y. Chen, W. Yan, G. Yue, and W. Zhou, "Multi-resolution hybrid explicit representation for novel view synthesis of dynamic scenes," *IEEE Transactions on Intelligent Vehicles*, pp. 1–11, 2024.

[27] R.-S. Wang and Y. Wang, "Multiview video sequence analysis, compression, and virtual viewpoint synthesis," *IEEE Transactions on Circuits and Systems for Video Technology*, vol. 10, no. 3, pp. 397–410, 2000.

[28] K. Deng, A. Liu, J.-Y. Zhu, and D. Ramanan, "Depth-supervised NeRF: Fewer views and faster training for free," in *CVPR*, June 2022.

[29] S. Guo, Q. Wang, Y. Gao, R. Xie, L. Li, F. Zhu, and L. Song, "Depth-guided robust point cloud fusion nerf for sparse input views," *IEEE Transactions on Circuits and Systems for Video Technology*, 2024.

[30] C. Song, S. Wang, J. Wei, and Y. Zhao, "Fewarnet: An efficient few-shot view synthesis network based on trend regularization," *IEEE Transactions on Circuits and Systems for Video Technology*, vol. 34, no. 10, pp. 9264–9280, 2024.

[31] M. Niemeyer, J. T. Barron, B. Mildenhall, M. S. M. Sajjadi, A. Geiger, and N. Radwan, "Regnerf: Regularizing neural radiance fields for view synthesis from sparse inputs," in *CVPR*, 2022.

[32] J. Song, M.-S. Kwak, and S. Kim, "Neural radiance fields with geometric consistency for few-shot novel view synthesis," 2022.

[33] Z. Liu, J. Su, G. Cai, Y. Chen, B. Zeng, and Z. Wang, "Georgs: Geometric regularization for real-time novel view synthesis from sparse inputs," *IEEE Transactions on Circuits and Systems for Video Technology*, 2024.

[34] J. Yang, M. Pavone, and Y. Wang, "Freenerf: Improving few-shot neural rendering with free frequency regularization," in *Proceedings of the IEEE/CVF Conference on Computer Vision and Pattern Recognition*, 2023, pp. 8254–8263.

[35] Q. Xu, X. Yi, J. Xu, W. Tao, Y.-S. Ong, and H. Zhang, "Few-shot nerf by adaptive rendering loss regularization," in *European Conference on Computer Vision*. Springer, 2025, pp. 125–142.

[36] Z. Zhu, Z. Fan, Y. Jiang, and Z. Wang, "Fsgs: Real-time few-shot view synthesis using gaussian splatting," 2023.

[37] W. Xu, H. Gao, S. Shen, R. Peng, J. Jiao, and R. Wang, "Mvpgs: Excavating multi-view priors for gaussian splatting from sparse input views," *arXiv preprint arXiv:2409.14316*, 2024.

[38] J. Li, J. Zhang, X. Bai, J. Zheng, X. Ning, J. Zhou, and L. Gu, "Dngaussian: Optimizing sparse-view 3d gaussian radiance fields with global-local depth normalization," in *Proceedings of the IEEE/CVF Conference on Computer Vision and Pattern Recognition*, 2024, pp. 20 775–20 785.

[39] R. Yin, V. Yugay, Y. Li, S. Karaoglu, and T. Gevers, "Fewviewgs: Gaussian splatting with few view matching and multi-stage training," *arXiv preprint arXiv:2411.02229*, 2024.

[40] R. Peng, W. Xu, L. Tang, L. Liao, J. Jiao, and R. Wang, "Structure consistent gaussian splatting with matching prior for few-shot novel view synthesis," in *Thirty-Eighth Conference on Neural Information Processing Systems (NeurIPS)*, 2024.

[41] R. Ranftl, A. Bochkovskiy, and V. Koltun, "Vision transformers for dense prediction," in *Proceedings of the IEEE/CVF international conference on computer vision*, 2021, pp. 12 179–12 188.

[42] S. Peng, X. Zhou, Y. Liu, H. Lin, Q. Huang, and H. Bao, "Pvnet: Pixel-wise voting network for 6dof object pose estimation," *IEEE Transactions on Pattern Analysis & Machine Intelligence*, vol. 44, no. 06, pp. 3212–3223, 2022.

[43] C. Zhong, C. Yang, F. Sun, J. Qi, X. Mu, H. Liu, and W. Huang, "Sim2real object-centric keypoint detection and description," in *Proceedings of the AAAI Conference on Artificial Intelligence*, vol. 36, no. 5, 2022, pp. 5440–5449.

[44] J. Sun, Z. Wang, S. Zhang, X. He, H. Zhao, G. Zhang, and X. Zhou, "Onepose: One-shot object pose estimation without cad models," in *Proceedings of the IEEE/CVF Conference on Computer Vision and Pattern Recognition*, 2022, pp. 6825–6834.

[45] F. Li, S. R. Vutukur, H. Yu, I. Shugurov, B. Busam, S. Yang, and S. Ilic, "Nerf-pose: A first-reconstruct-then-regress approach for weakly-supervised 6d object pose estimation," in *Proceedings of the IEEE/CVF International Conference on Computer Vision*, 2023, pp. 2123–2133.

[46] J. Y. Zhang, D. Ramanan, and S. Tulsiani, "Relpose: Predicting probabilistic relative rotation for single objects in the wild," in *European Conference on Computer Vision*. Springer, 2022, pp. 592–611.

[47] A. Lin, J. Y. Zhang, D. Ramanan, and S. Tulsiani, "Relpose++: Recovering 6d poses from sparse-view observations," *arXiv preprint arXiv:2305.04926*, 2023.

[48] C. Sun, M. Sun, and H.-T. Chen, "Direct voxel grid optimization: Super-fast convergence for radiance fields reconstruction," in *Proceedings of the IEEE/CVF Conference on Computer Vision and Pattern Recognition*, 2022, pp. 5459–5469.

[49] B. Mildenhall, P. P. Srinivasan, M. Tancik, J. T. Barron, R. Ramamoorthi, and R. Ng, "NeRF: Representing scenes as neural radiance fields for view synthesis," in *ECCV*, 2020.

[50] P. Wang, L. Liu, Y. Liu, C. Theobalt, T. Komura, and W. Wang, "Neus: Learning neural implicit surfaces by volume rendering for multi-view reconstruction," *arXiv preprint arXiv:2106.10689*, 2021.

[51] M. M. Johari, Y. Lepoittevin, and F. Fleuret, "Geonerf: Generalizing nerf with geometry priors," *arXiv preprint arXiv:2111.13539*, 2021.

[52] T. Wu, J. Wang, X. Pan, X. Xu, C. Theobalt, Z. Liu, and D. Lin, "Voxurf: Voxel-based efficient and accurate neural surface reconstruction," *arXiv preprint arXiv:2208.12697*, 2022.

[53] Q. Fu, Q. Xu, Y. S. Ong, and W. Tao, "Geo-neus: Geometry-consistent neural implicit surfaces learning for multi-view reconstruction," *Advances in Neural Information Processing Systems*, vol. 35, pp. 3403–3416, 2022.

[54] Y. Deng, J. Yang, and X. Tong, "Deformed implicit field: Modeling 3d shapes with learned dense correspondence," in *Proceedings of the IEEE/CVF Conference on Computer Vision and Pattern Recognition*, 2021, pp. 10 286–10 296.

[55] D. DeTone, T. Malisiewicz, and A. Rabinovich, "Superpoint: Self-supervised interest point detection and description," 2018.

[56] P.-E. Sarlin, D. DeTone, T. Malisiewicz, and A. Rabinovich, "Superglue: Learning feature matching with graph neural networks," in *CVPR*, 2020.

[57] M. Oechsle, S. Peng, and A. Geiger, "Unisurf: Unifying neural implicit surfaces and radiance fields for multi-view reconstruction," in *Proceedings of the IEEE/CVF International Conference on Computer Vision*, 2021, pp. 5589–5599.

[58] C. Tang and P. Tan, "Ba-net: Dense bundle adjustment network," *arXiv preprint arXiv:1806.04807*, 2018.

[59] K. Simonyan and A. Zisserman, "Very deep convolutional networks for large-scale image recognition," in *3rd International Conference on Learning Representations (ICLR 2015)*. Computational and Biological Learning Society, 2015.

[60] J. Engel, V. Koltun, and D. Cremers, "Direct sparse odometry," *IEEE transactions on pattern analysis and machine intelligence*, vol. 40, no. 3, pp. 611–625, 2017.

[61] J. T. Barron, B. Mildenhall, D. Verbin, P. P. Srinivasan, and P. Hedman, "Mip-nerf 360: Unbounded anti-aliased neural radiance fields," *CVPR*, 2022.

[62] A. Gropp, L. Yariv, N. Haim, M. Atzmon, and Y. Lipman, "Implicit geometric regularization for learning shapes," *arXiv preprint arXiv:2002.10099*, 2020.

[63] B. Yang, Y. Zhang, Y. Xu, Y. Li, H. Zhou, H. Bao, G. Zhang, and Z. Cui, "Learning object-compositional neural radiance field for editable scene rendering," in *International Conference on Computer Vision (ICCV)*, October 2021.

[64] R. Jensen, A. Dahl, G. Vogiatzis, E. Tola, and H. Aanæs, "Large scale multi-view stereopsis evaluation," in *Proceedings of the IEEE conference on computer vision and pattern recognition*, 2014, pp. 406–413.

[65] J. Straub, T. Whelan, L. Ma, Y. Chen, E. Wijmans, S. Green, J. J. Engel, R. Mur-Artal, C. Ren, S. Verma, A. Clarkson, M. Yan, B. Budge, Y. Yan, X. Pan, J. Yon, Y. Zou, K. Leon, N. Carter, J. Briales, T. Gillingham, E. Mueggler, L. Pesqueira, M. Savva, D. Batra, H. M. Strasdat, R. D. Nardi, M. Goesele, S. Lovegrove, and R. Newcombe, "The Replica dataset: A digital replica of indoor spaces," *arXiv preprint arXiv:1906.05797*, 2019.

[66] M. Denninger, D. Winkelbauer, M. Sundermeyer, W. Boerdijk, M. Knauer, K. H. Strobl, M. Humt, and R. Triebel, "Blenderproc2: A procedural pipeline for photorealistic rendering," *Journal of Open Source Software*, vol. 8, no. 82, p. 4901, 2023. [Online]. Available: https://doi.org/10.21105/joss.04901

[67] A. Handa, V. Pătrăucean, S. Stent, and R. Cipolla, "Scenenet: An annotated model generator for indoor scene understanding," in *2016 IEEE International Conference on Robotics and Automation (ICRA)*. IEEE, 2016, pp. 5737–5743.

[68] A. X. Chang, T. Funkhouser, L. Guibas, P. Hanrahan, Q. Huang, Z. Li, S. Savarese, M. Savva, S. Song, H. Su *et al.*, "Shapenet: An information-rich 3d model repository," *arXiv preprint arXiv:1512.03012*, 2015.

[69] Z. Wang, A. C. Bovik, H. R. Sheikh, and E. P. Simoncelli, "Image quality assessment: from error visibility to structural similarity," *IEEE transactions on image processing*, vol. 13, no. 4, pp. 600–612, 2004.

[70] R. Zhang, P. Isola, A. A. Efros, E. Shechtman, and O. Wang, "The unreasonable effectiveness of deep features as a perceptual metric," in *CVPR*, June 2018.

[71] A. Krizhevsky, I. Sutskever, and G. E. Hinton, "Imagenet classification with deep convolutional neural networks," *Advances in neural information processing systems*, vol. 25, 2012.

[72] A. Kirillov, E. Mintun, N. Ravi, H. Mao, C. Rolland, L. Gustafson, T. Xiao, S. Whitehead, A. C. Berg, W.-Y. Lo, P. Dollár, and R. Girshick, "Segment anything," *arXiv:2304.02643*, 2023.

[73] J. Zhang, G. Yang, S. Tulsiani, and D. Ramanan, "Ners: Neural reflectance surfaces for sparse-view 3d reconstruction in the wild," *Advances in Neural Information Processing Systems*, vol. 34, pp. 29 835–29 847, 2021.

Zhirui Gao received his B.E. degree in computer science and technology from China University of Geosciences, Wuhan in 2021. He is now a Ph.D. Student at the National University of Defense Technology, China. His research interests include computer graphics and 3D vision.

Renjiao Yi is an Associate Professor at the School of Computer, National University of Defense Technology. She received her Ph.D. degree from Simon Fraser University in 2019. She is interested in inverse rendering, 3D scene understanding & editing, and related AR applications.

Chenyang Zhu is an Associate Professor at the School of Computer, National University of Defense Technology. The current directions of interest include data-driven shape analysis and modeling, 3D vision and, robot perception & navigation, etc.

Ke Zhuang received her B.E. degree in computer science and technology from China Jiliang University in 2023. She is now a graduate student at the National University of Defense Technology, China. Her research interests include computer vision and generative models.

Wei Chen is a Professor at the School of Computer, National University of Defense Technology. Her current research interests include computer architecture, artificial intelligence, and computer vision.

Kai Xu (Senior Member, IEEE) received the Ph.D. degree in computer science from the National University of Defense Technology (NUDT), Changsha, China, in 2011. From 2008 to 2010, he worked as a Visiting Ph.D. degree with the GrUVi Laboratory, Simon Fraser University, Burnaby, BC, Canada. He is currently a Professor with the School of Computer Science, NUDT. He is also an Adjunct Professor with Simon Fraser University. His research interests include data-driven shape analysis and modeling, and 3D vision and robot perception and navigation.